Tectonics®

RESEARCH ARTICLE
10.1029/2024TC008475

Recent Block Kinematics and Fault Slip Rates in the Pamir, Central Asia, From an Integrated GNSS Velocity Field

Dongzhen Wang[1], Bin Zhao[1], Jie Li[2], Sabrina Metzger[3], Chong Gu[1], Wei Wang[1], Gang Zheng[4], Jiansheng Yu[1], and Xuejun Qiao[1]

[1]Key Laboratory of Earthquake Geodesy, Institute of Seismology, China Earthquake Administration, Wuhan, China, [2]Earthquake Administration of the Xinjiang Uygur Autonomous Region, China Earthquake Administration, Urumqi, China, [3]Helmholtz Centre Potsdam, GFZ German Research Centre for Geosciences, Potsdam, Germany, [4]COMET, School of Earth and Environment, University of Leeds, Leeds, UK

Key Points:

- The recent surface velocity field suggests the Pamir plateau to be subdivided into three EW-extending micro-blocks
- The NNE-striking Sarez-Karakul fault system accommodates significant sinistral shear and most probably continues further toward (S)SW
- EW-extension in the Pamir increases northward with maximum extension close to the Pamir thrust front

Supporting Information:

Supporting Information may be found in the online version of this article.

Correspondence to:

B. Zhao,
zhaobin@cgps.ac.cn

Citation:

Wang, D., Zhao, B., Li, J., Metzger, S., Gu, C., Wang, W., et al. (2024). Recent block kinematics and fault slip rates in the Pamir, Central Asia, from an integrated GNSS velocity field. *Tectonics*, *43*, e2024TC008475. https://doi.org/10.1029/2024TC008475

Received 8 JUL 2024
Accepted 8 OCT 2024

Author Contributions:

Conceptualization: Bin Zhao
Data curation: Dongzhen Wang, Jie Li, Sabrina Metzger
Formal analysis: Sabrina Metzger, Wei Wang, Gang Zheng, Jiansheng Yu, Xuejun Qiao
Funding acquisition: Xuejun Qiao
Methodology: Dongzhen Wang, Bin Zhao, Jie Li, Jiansheng Yu
Software: Gang Zheng
Supervision: Bin Zhao
Validation: Chong Gu, Jiansheng Yu
Visualization: Dongzhen Wang, Chong Gu
Writing – original draft: Dongzhen Wang, Bin Zhao, Sabrina Metzger, Wei Wang

Abstract Contemporary kinematic characteristics of the Pamir plateau are characterized by (a) significant NS-shortening across the northern front, (b) EW-extension within the Pamir and (c) gravitationally driven westward mass-outflux of the western Pamir into the Tajik basin. The 2015 Mw 7.2 Sarez and 2023 Mw 6.8 Murghab strike-slip earthquakes highlight the crucial role of shear deformation in the Pamir's interior, but the detailed secular kinematics of the remote Plateau are still elusive. Here, we employ elastic block models to fit GNSS velocities compiled from our own reprocessed velocity solution and from previous studies to determine slip rates along major active faults within and bounding the Pamir plateau. Our favored model separates the Pamir's interior into three micro-blocks along the NNE-trending sinistral Sarez-Karakul fault system and the SSE-trending Kongur Shan extensional system. The model confirms significant crustal shortening along the Pamir's northern boundary and strike-slip motion along its western boundary, namely the Pamir thrust system and the Darvaz fault, respectively. In contrast, strike-slip motion on the eastern boundary is minor. In the interior of the Plateau, we find an upper limit of sinistral shear of 8.8 ± 0.3–9.5 ± 0.2 mm/yr along the Sarez-Karakul fault system and dextral shear of 6.3 ± 0.3 mm/yr along the WNW-trending Muji fault. Our model also confirms recent observations of an active, SW-continuation of the Sarez-Karakul fault system. In the eastern Pamir, crustal extension mainly occurs across the northern segment of the Kongur Shan extensional system. The recent large strike-slip earthquakes on the Pamir plateau suggest that shear motion on the plateau is accommodated on a much wider range than only by the Sarez-Karakul fault system.

1. Introduction

The arcuate Pamir, located in the western Himalayan syntaxis, is one of the most active continental collision zones. It is bounded by the Tarim basin to the east and Tajik basin to the west, which were once connected by an early Cenozoic basin (Figure 1; Burtman & Molnar, 1993; Strecker et al., 1995). The tectonic evolution of the Pamir is primarily characterized by terrane accretion, significant deformation, and northward overthrusting caused by the ongoing convergence between the India indenter and the Eurasian plate (e.g., Burtman & Molnar, 1993). The northward advance of the Pamir progressively closed the Cenozoic basin to a narrow intramontane basin, the Alai valley (e.g., Arrowsmith & Strecker, 1999). The Pamir thrust system absorbs most of the NS convergence between Pamir and southwestern Tian Shan. To the east, the Kashgar-Yecheng transfer system accommodates dextral shear between the Pamir and Tarim basin. To the west, the sinistral Darvaz fault marks the boundary to the Tajik basin. Crustal extension within the Pamir is emphasized along the NNE-trending sinistral-transtensional Sarez-Karakul fault system (e.g., Strecker et al., 1995) and the SSE-trending Kongur Shan extensional system. A variety of features, including thickened crust of over 60 km (e.g., Schneider et al., 2013), and elevated surface heat flow (Sass et al., 2014), imply that the Pamir is a mature orogen similar to the Tibetan Plateau (e.g., Sippl et al., 2013). It is recognized as an ideal place to study the ongoing subduction of continental lithosphere, where deep Indian plate meets deep Asian plate, as imaged by intermediate-depth seismicity beneath the Pamir and the adjacent Hindu Kush further SW (e.g., Kufner et al., 2016, 2021; Figure 1b).

Slip rate constraints of the active faults bounding the Pamir have been relatively well documented with geological (e.g., Arrowsmith & Strecker, 1999; Chevalier et al., 2011, 2015; Coutand et al., 2002; Trifonov, 1978) and instrumental evidence (e.g., Ischuk et al., 2013; Metzger et al., 2020; Mohadjer et al., 2010; Zhou et al., 2016; Zubovich et al., 2010, 2016). But the crustal deformation in Pamir's interior is rarely documented. Extensional

Writing – review & editing: Bin Zhao, Sabrina Metzger

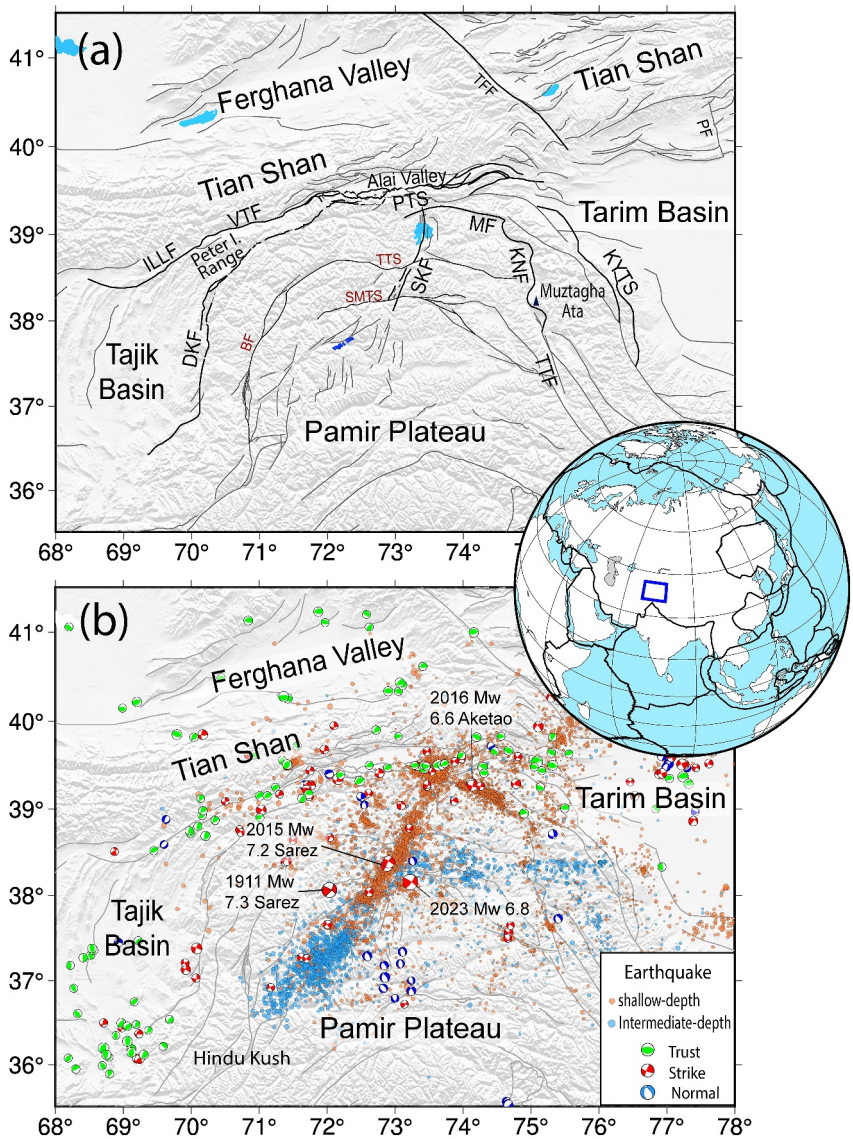

Figure 1. (a) Tectonic setting of the Pamir region. Black lines indicate active faults (Mohadjer et al., 2016) used to constrain the block model geometry. Abbreviations: BF, Badakhshan Fault; DF, Darvaz fault; ILLF, Illiac fault; KNF, Kongur Shan normal fault; KYTS, Kashgar-Yecheng transfer system; MF, Muji fault; PF, Piqiang fault; PTS, Pamir thrust system; SKF, Sarez-Karakul fault system; SMTS, Sarez-Murghab thrust system; TFF, Talas Ferghana fault; TTF, Tashkorgan and Taheman fault; TTS, Tanymas thrust system; VTF, Vakhsh thrust fault. Blue dotted lines mark the southwestward extension of the SKF suggested by Elliott et al. (2020). (b) Seismicity in the Pamir and surrounding area. Beach balls represent focal mechanisms of shallow crustal (≤40 km) earthquakes released by the Global Centroid Moment Tensor project (GCMT, Ekström et al., 2012). Focal mechanism for the 1911 earthquake is from Kulikova et al. (2016). Blue, red and green beach balls indicate normal, strike-slip and thrust faulting mechanisms, respectively. Orange and blue small circles represent shallow earthquakes (Bloch et al., 2023), and intermediate-depth earthquakes (between 50 and 250 km, Sippl et al., 2013), respectively. Blue box and thick black lines in the inset globe show the study area and plate boundaries (Bird, 2003), respectively.

deformation across the Kongur Shan normal fault and the Sarez-Karakul normal fault system has been emphasized since the study by Burtman and Molnar (1993). The Kongur Shan extensional system (from north to south) consists of the WNW-trending Muji fault, the SSE-trending Kongur Shan normal fault, and the Taheman-Tashkorgan normal faults (Figure 1; Chevalier et al., 2015; Robinson et al., 2007). In 2016, the Mw 6.6 Aketao earthquake ruptured the Muji fault with a predominant dextral strike-slip mechanism (e.g., Feng et al., 2017; S. Wang et al., 2017; W. Wang et al., 2017). Using offset stream channels and fault scarps across

Lake Karakul, Strecker et al. (1995) mapped the northern segment of the Sarez-Karakul as a sinistral-transtensional fault. Based on recent fieldwork, as well as interpretation of optical images and digital elevation models, Schurr et al. (2014) showed that the fault could be traced northward to its intersection with the Pamir thrust system, while Elliott et al. (2020) found evidence of a southward extension (marked in blue in Figure 1a) nearly into the Afghan Hindu Kush. Based on the distinct contrast in seismicity and morphotectonic features between the western and eastern Pamir, Schurr et al. (2014) proposed that the Pamir is separated by the Sarez-Karakul fault system, acting as a surface expression of the Indian indenter at depth (Kufner et al., 2018; Metzger et al., 2017). The 2015 moment magnitude (Mw) 7.2 sinistral Sarez earthquake (Figure 1b; Metzger et al., 2017; Sangha et al., 2017) supports the inference of Schurr et al. (2014). Recent findings, however, suggest that shear motion is distributed across a broader zone. The 1911 M ∼ 7.7 Sarez earthquake, with a similar rupture mechanism, is thought to have occurred either on ∼100 km west of the Sarez-Karakul fault system (Kulikova et al., 2016) or on its southwestward extension (Elliott et al., 2020), and the 2023 Mw 6.8 Murghab earthquake ruptured an unmapped strike-slip fault located ∼20 km east of and parallel to the Sarez-Karakul fault system (Figure 1; R. Chen et al., 2024; Shi et al., 2023). These three large earthquakes along with the 2016 Aketao earthquake highlight the poorly understood but complex shear processes in the Pamir's interior (R. Chen et al., 2024; Kulikova et al., 2016; Metzger et al., 2017; Sangha et al., 2017; Shi et al., 2023). Recent field efforts aimed at refining crustal velocity field and better understanding strain partitioning in the Pamir region significantly increased the number of Global Navigation Satellite System (GNSS) observation stations in this remote region (Ischuk et al., 2013; Metzger et al., 2020; Mohadjer et al., 2010; Perry et al., 2019; Zhou et al., 2016; Zubovich et al., 2010).

While Perry et al. (2019) utilized elastic block modeling to find the major shortening axis between the Asian and Indian continents, we aim to identify the active crustal blocks and faults bounding the Pamir's interior and constrain their kinematics. To do so, we first integrated the GNSS velocities from most of the aforementioned GNSS effects with new survey-mode GNSS data of western China to obtain an updated and unified velocity field over the whole Pamir (Section 3). We then designed block models primarily constrained by geologic, geodetic, and seismic evidence of active faults (Figure 1b and Section 2) and fitted them to the observed GNSS velocities (Sections 4 and 5). One model scenario contains a single Pamir block similarly to previous studies (e.g., Zhou et al., 2016), while the other three models consider an active Sarez-Karakul fault system and/or the Kongur Shan extensional system. We tested the performance of these models by weighting model complexity against GNSS data fit (AIC and AICc) (Akaike, 1974). Finally, we compared our model results—Euler poles, a homogeneous velocity and strain-rate field, and derived fault slip rates—to published models and geodetic and geologic observations, and proposed an updated conceptual model of the kinematics in the Pamir plateau (Section 6).

2. Quaternary and Geodetic Fault Slip Rates

The following compilation of active fault kinematics outlines the primary crustal deformation zones that subsequently delineate the boundaries of our kinematic model blocks. We provide an overview of fault slip rates along the fault systems bounding the Tajik basin to the north (Illiac and Vakhsh faults), the Pamir plateau toward west, north and east (Darvaz fault, Pamir thrust system, Kashgar-Yecheng transfer system), and, finally, the two fault systems that subdivide the Pamir's interior (Sarez-Karakul fault system and Kongur Shan extensional system) (Figure 1a).

The E to ENE-trending, dextral-reverse Illiac fault separates the Tajik basin from the southwestern Tian Shan (Kufner et al., 2018; Schurr et al., 2014). It links to the ENE-trending, dextral-transpressive Vakhsh thrust fault that splays itself from the E-trending Pamir thrust system and separates the western Pamir from the southwestern Tian Shan (Figure 1). The Illiac fault exhibits shortening of ∼5 mm/yr and dextral shear of 8–15 mm/yr (Metzger et al., 2020). The Vakhsh fault accommodates the crustal shortening and dextral shear between the Tajik basin and the southwestern Tian Shan (Burtman & Molnar, 1993; Trifonov, 1983). While early estimates of geodetic slip rates of the Vakhsh fault (16 ± 1 mm/yr, Guseva, 1986; Konolpatsev, 1971) were possibly affected due to the postseismic effects following the 1949, Mw7.6 Khait earthquake, a more recent GNSS study presented a wide range of shortening between 12 and 19 mm/yr and dextral shear between 13 and 19 mm/yr (Metzger et al., 2020). Both the Illiac and Vakhsh faults appear to have very shallow locking depths, probably due to the abundance of low-friction evaporites in the region (Metzger et al., 2020; Nikolaev, 2002).

The sinistral-transpressive Darvaz fault defines the boundary between the Pamir and the Tajik basin and forks—together with the dextral-transpressive Vakhsh thrust but in a more SW- and then S-striking sense and thereby

embracing the seismically active Peter I. Range (Figure 1)—from the Pamir thrust system (Burtman & Molnar, 1993). Its Quaternary sinistral shear rate was estimated to be 10–15 mm/yr along the southern segment of the Darvaz fault at ∼37.8°N (Trifonov, 1978), with relatively large uncertainty due to the difficulty of dating the offset geomorphological features (Trifonov, 1978). Using velocities from a sparse GNSS network, Ischuk et al. (2013) and Mohadjer et al. (2010) found ∼10 mm/yr sinistral shear over a distance of ∼250 km. Recently, based on two dense GNSS profiles crossing the Darvaz fault and elastic dislocation models, Metzger et al. (2020) suggested that sinistral shear decreases along-strike from ∼15 mm/yr at ∼38.8°N to 7–9 mm/yr at ∼38°N. Where the Darvaz fault and Vakhsh fault run in parallel, the westward collapse and simultaneous northward advance of the Pamir cause convergence and abundant seismicity (Figure 1).

The western segment of the E-trending Pamir thrust system accommodates instrumental shortening rates of 12–13 mm/yr and shear rates of 5–6 mm/yr (Ischuk et al., 2013; Zubovich et al., 2010, 2016, 2022), which are slightly higher than the Holocene dextral slip rate of 2.5–6 mm/yr derived by Arrowsmith and Strecker (1999), but lower than the estimated Cenozoic shortening rate of ∼20 mm/yr (Burtman & Molnar, 1993). Toward the eastern segment, shortening rates increase to 10–15 mm/yr, while dextral shear rates remain at 5–6 mm/yr (Zubovich et al., 2010, 2016, 2022), indicating that the eastern Pamir is unaffected by the westward gravitational collapse of the western Pamir into the Tajik basin (Metzger et al., 2020; Schurr et al., 2014). Overall, the Pamir thrust system absorbs more than one-third of the total convergence between India and Asia (∼35 mm/yr).

The NWW-trending dextral-transpressive Kashgar-Yecheng transfer system has accumulated approximately 280 km of northward offset of the Pamir relative to the Tarim basin, first, at a rate of 11–15 mm/yr during the late Cenozoic (Cowgill, 2010), then at a slower rate of 1.7–5.3 mm/yr since ∼5 Ma due to the substantial northward acceleration of the Tarim basin (Sobel et al., 2011). Recent, albeit sparse GNSS observations suggest that the transfer system is currently inactive (Ischuk et al., 2013; Zhou et al., 2016).

In the Pamir's interior, GNSS rates indicate that the Sarez-Karakul fault system accommodates 5 ± 2 mm/yr of sinistral shear and 1–3 mm/yr of extension (Metzger et al., 2020). The Muji fault exhibits a Holocene strike-slip rate ranging from 4.5 ± 0.2 to 11.1 ± 0.9 mm/yr, most probably at a maximum of ∼7 mm/yr (Chevalier et al., 2011). Recently, T. Li et al. (2019) refined the Holocene dextral-slip rate to 6–9 mm/yr. Based on GNSS data, Feng et al. (2017) reported a dextral shear of 9.4 ± 2.5 mm/yr, which is close the upper limit constrained by geological data. The Kongur Shan extensional system exhibits Holocene extension of 6–8 mm/yr at its northern end (J. Chen et al., 2011) and ∼3–5 mm/yr in recent times (Ischuk et al., 2013; Zhou et al., 2016).

3. GNSS Data Integration and Processing

The number of individual GNSS velocity solutions in the Pamir region is steadily growing (Ischuk et al., 2013; Jouanne et al., 2014; Kufner et al., 2021; Metzger et al., 2020; Mohadjer et al., 2010; Perry et al., 2019; Zhou et al., 2016; Zubovich et al., 2010). These data sets cover most of the Pamir plateau and surrounding regions but GNSS observations from the Pamir's eastern rim and western China are sparse. We collected raw GNSS data from 149 stations of the Crustal Movement Network of China (CMONOC), 8 stations installed by the Earthquake Administration of Xinjiang Uygur Autonomous Region and 25 stations located in the western Pamir and Tajik basin surveyed by Metzger et al. (2020). The observation time spans for all GNSS stations are summarized along with the velocities (see Data Availability Statement). We processed these data using the GAMIT/GLOBK software version 10.7 (Herring et al., 2018) to obtain loosely constrained daily solutions (Zhao et al., 2015), incorporating empirical GPT2 tropospheric slant delay model (Lagler et al., 2013) and the latest absolute antenna phase center model in the international terrestrial reference ITRF2014 (Altamimi et al., 2016). We then estimated long-term rates, offsets caused by earthquake and instrument changes, and seasonal terms (for continuous time series) from the position time series using least squares (Herring et al., 2018). Finally, we transformed the GNSS velocities into a stable Eurasian reference frame using the Euler vector described in Altamimi et al. (2017).

In order to generate an unified GNSS velocity solution for the whole study region, we then integrated previously published data sets (Ischuk et al., 2013; Jouanne et al., 2014; Perry et al., 2019; Zhou et al., 2016; Zubovich et al., 2010) into our velocity solution by a six-parameter Helmert transformation (rotation and translation). Differences of the common stations are generally smaller than 1.0 mm/yr. We rejected anomalous velocities of Perry et al. (2019) that were affected by more than 3.0 mm of coseismic offsets of the 2015 Mw 7.2 Sarez earthquake (Figure S1; Table S1 in Supporting Information S1; personal communication M. Perry in 2019). For

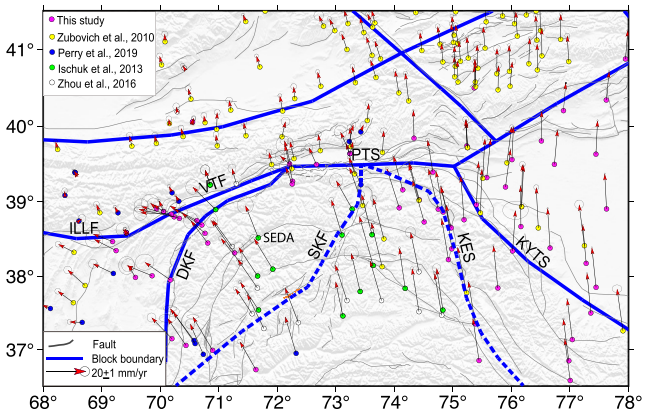

Figure 2. Compilation of GNSS velocities (with 95% confidence level) from previous studies as well as our own solutions, relative to stable Eurasia. Blue lines represent the block model geometry, where the Pamir either comprises one (model 1), two (model 2A and 2B, including one of the two dashed lines) or three micro-blocks (model 3, including both dashed lines). Gray lines represent active faults (Mohadjer et al., 2016). Orange dotted lines mark the southwestward extension of the Sarez-Karakul fault system suggested by Elliott et al. (2020). Abbreviation: KES, Kongur Shan extensional system. See Figure 1 for other fault abbreviations.

example, the velocity at station SEDA from Perry et al. (2019) differs by 8 mm/yr from a prior solution of Zubovich et al. (2010). Most rejected velocities from Perry et al. (2019) exist, however, in earlier solutions of Zubovich et al. (2010) and Ischuk et al. (2013) that are unaffected by the 2015 earthquake. Our compilation consists of 547 horizontal GNSS velocities, of which 217 stations are located in the study region (Figure S2 in Supporting Information S1), representing the most complete GNSS velocity field in the Pamir region so far (Figure 2), particularly in the interior of the Pamir. In the study area, the average uncertainties are 0.5 and 0.7 mm/yr in the east and north components, respectively. The GNSS velocities nicely depict the overall northward motion of the Pamir, with distinguishable lateral motion components at the western and eastern rims.

4. Elastic Block Model and Fault Slip Inversion

4.1. Block Modeling Approach

Block model analysis of secular velocity field is a convenient method for determining first-order kinematic parameters of major tectonic structures, such as crustal block rotation and fault slip rates (e.g., Meade & Loveless, 2009). In a traditional block model, secular velocities result from the integration of block rotation, the cumulative slip deficit at the block boundaries, and, optionally, additional velocity gradients due to uniform strain within the blocks (e.g., Loveless & Meade, 2011; McCaffrey, 2005; Meade & Hager, 2005; Meade & Loveless, 2009),

$$v = \Omega \times r - \sum_{f=1}^{N_{\text{faults}}} G \cdot s + G_{\dot{\varepsilon}} \cdot \dot{\varepsilon} \quad (1)$$

where v is the predicted interseismic velocity. Ω is the rotation vector of micro-block, r is the position of GNSS station. G and $G_{\dot{\varepsilon}}$ are elastic Green's functions relating fault slip s on each segment (Okada, 1985) and block internal strain rate $\dot{\varepsilon}$ to velocities at GNSS stations, respectively. N_{faults} is the number of faults bounding the micro-blocks. The first term on the right side of Equation 1 represents the block rotation, the second is the cumulative slip deficit due to the fault slip on all segments, and the third represents block-internal strain rate.

To avoid unrealistic estimate of block rotations, we only account for block rotation and elastic strain accumulation on the locked portion of the faults and resolve for the three rotation components for each block using the Blocks software (Meade & Loveless, 2009). The unified GNSS velocities with their formal uncertainties are used to estimate the Euler vectors, and the slip rates on the faults are determined by the relative rotation between neighboring blocks. The formal slip rate uncertainties are primarily related to velocity uncertainties and do not reflect the uncertainties in fault system geometry (Meade & Hager, 2005).

4.2. Block Geometries

Block boundaries are generally parameterized based on a combination of mapped fault traces, relocated seismicity, topographic lineaments, geological cross sections (e.g., d'Alessio et al., 2005), and GNSS velocity gradients (Shen et al., 2005; Xu et al., 2008). For the Pamir plateau specifically, we consulted the Quaternary fault data base of Central Asia (Mohadjer et al., 2016) and crustal seismicity, including relocated foreshocks, mainshocks and aftershocks during the period from 2015 to 2017 (Bloch et al., 2023). In particular, we focused on seismic activity associated with the 2015 Sarez earthquake on the Sarez-Karakul fault system and the 2016 Aketao earthquake on the Muji fault, both located within the Pamir's interior (Figure 1b). Beyond the Pamir plateau, micro-blocks are defined by a series of bounding faults, such as the Pamir thrust system in the north, the Darvaz fault to the west, the Kashgar-Yecheng transfer system to the east and further northwest, the Talas Ferghana fault, among others (Figure 1).

We constructed four block model candidates that only differ in the number of Pamir sub-blocks (Figure 2). Model 1 describes the Pamir as a single block. While model 2A divides the eastern and western Pamir along the Sarez-Karakul fault system, model 2B divides the Pamir along the Kongur Shan extensional system. Model 3 unites model 2A and 2B to be a three micro-blocks. Based on optical image analysis and analog seismogram models, Elliott et al. (2020) suggested that the SW-extension of the Sarez-Karakul fault system potentially hosted the 1911 earthquake. To test this and identify the best location of the micro-block boundaries of model 2A, we performed an initial cluster analysis of the GNSS velocities within the Pamir (Simpson et al., 2012; Figure S3 in Supporting Information S1) and found that the optimal block boundary nicely aligns with the streak of the intermediate-depth earthquakes (Figure 1b; Sippl et al., 2013). Given the GNSS data sparsity, we did not consider the unmapped fault that ruptured during the 2023 Mw 6.8 Murghab earthquake in our block model, as the rupture mechanism and fault strike are poorly constrained (R. Chen et al., 2024; Shi et al., 2023). Similarly, due to data sparsity, we excluded the Cenozoic Tanymas thrust system, the likely active Sarez-Murghab thrust system (Schurr et al., 2014) and the Badakhshan fault (labeled in red in Figure 1a). Initial tests of more complex models incorporating the aforementioned faults did not further improve the data fit, suggesting that the block geometry considered here is reasonable.

Since most faults lack detailed structural information, we assumed a general fault dip of 20°, 45°, and 90° for thrust, normal and strike-slip faults (e.g., Perry et al., 2019). For the Sarez-Karakul fault system, however, we used an 87° westward-dipping fault plane constrained by coseismic slip inversion (Metzger et al., 2017; Sangha et al., 2017). Furthermore, we assumed that all faults are locked to 20 km depth, supported by the 95% maximum depth of shallow crustal earthquakes (Figure S4 in Supporting Information S1; d'Alessio et al., 2005). But to evaluate the influence of the predefined fault locking depth, we varied the locking depth from 10 to 30 km and evaluated its influence on slip rates and data misfit.

4.3. Model Evaluation Method

To find out whether the Pamir plateau kinematics are best described by one, two or three micro-blocks, we consult the Akaike Information Criterion (AIC) and a modified version of it (AICc) that evaluates the model misfit by incorporating statistical penalties for each additional model parameter (Akaike, 1974). We calculated the $\mathrm{AIC} = n\log\left(\sigma^2\right) + 2K$ and $\mathrm{AICc} = \mathrm{AIC} + \frac{2K(K+1)}{n-K-1}$, respectively, where n is the number of GNSS velocity observations, σ^2 is the weighted root-mean-square (WRMS) misfit determined from the model inversion, and K is the number of free model parameters. K increases by 3 with each additional block model boundary. A model with lower AIC(c) values should be favored over one with a larger AIC(c), and we only consider the Pamir-internal blocks and GNSS data in the AIC(c) calculations.

5. Results

5.1. Block Rotation Poles

The estimated Euler vectors for the Tajik basin, Tarim basin, Ferghana valley and Tian Shan remain unaffected by the different block model scenarios (Figure 3 and Figures S5–S7 in Supporting Information S1). The Tarim basin rotates clockwise relative to the stable Eurasia plate at an angular velocity of 0.62°/Myr around a pole located at 98.03°E and 37.88°N, the Tajik basin rotates counterclockwise at an angular rate of 1.62°/Myr around a pole at 67.91°E and 35.44°N. The southwestern Tian Shan and the Ferghana valley blocks (north of the Pamir) rotate around a similar pole and with similar angular velocities, implying that these blocks currently rotate as one (Evans et al., 2015). Whether these two blocks should be treated as a single larger block is beyond the scope of this study.

The Pamir micro-block rotations vary significantly depending on the number of blocks used (Figure 3 and Figures S5–S7 in Supporting Information S1). In the single-block model 1, the rotation pole lies further southwest than the pole determined by Zhou et al. (2016) in a similar model, likely because of the additional GNSS velocities in the eastern Pamir. If the Kongur Shan block is separated from the western and central Pamir (model 2B), the rotation vector agrees with the findings of Zhou et al. (2016).

In model 3, the Kongur Shan rotates counterclockwise at an angular velocity of 1.14°/Myr around 89.66°E and 37.61°N, which is ~800 km west of the Tarim basin's pole. The western Pamir pole rotates counterclockwise at 0.97°/Myr, which is five times faster that of the eastern Pamir. The eastern Pamir's pole is located at 18.62°E and

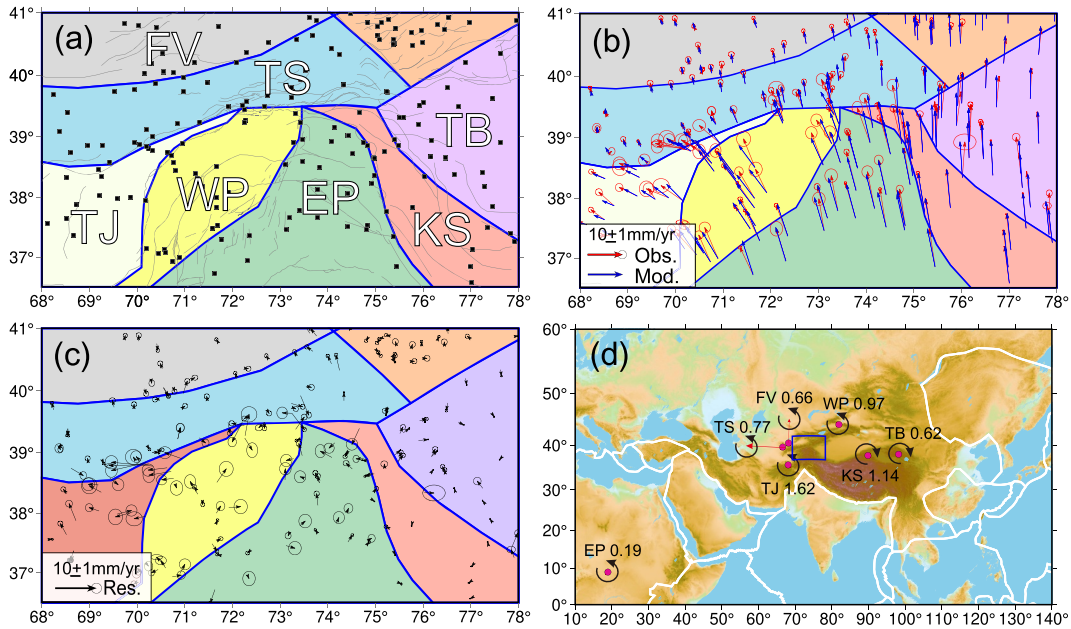

Figure 3. The preferred block model 3. (a) Block boundaries (blue) and GNSS station locations (black squares). (b) Comparison of the observed and predicted GNSS velocities with 95% confidence intervals. (c) Model residuals. (d) Euler poles and angular velocities (in °/Myr) along with global plate boundaries (white lines) (Bird, 2003) on topographic map. Blue box outlines the study area. Block abbreviations: EP, eastern Pamir; FV, Ferghana valley; TB, Tarim basin; TJ, Tajik basin; TS, southwestern Tian Shan; WP, western Pamir.

8.57°N (central Africa), indicating that the eastern Pamir exhibits predominant northward motion and little rotation (Figure 3d, Table 1).

5.2. Preferred Block Model

The single Pamir block model 1 drastically underestimates southwest directed motion of 5–10 mm/yr in the western Pamir (Figure S5 in Supporting Information S1) and products the highest WRMS and AIC(c) values (Table 2), suggesting the need of at least one additional micro-block. The data fit improves significantly when dividing the Pamir into two micro-blocks, either along the Sarez-Karakul fault zone (model 2A) (Figure S6 in Supporting Information S1) or the Kongur Shan extensional system (model 2B) (Figure S7 in Supporting Information S1). Model 2A results in a substantially better fit than model 2B, which still features similar, albeit smaller, systematic residual velocities like model 1 (~5 mm/yr) (Figure S6 in Supporting Information S1).

Table 1
Euler Poles of All Micro-Blocks With Respect to Stable Eurasia Constrained by Our Preferred Model 3

Block name	Number of sites	Longitude (°)	Latitude (°)	Rotation rate (°/Myr)	WRMS (mm/yr)
TJ	14	67.91 ± 0.28	35.44 ± 0.65	1.62 ± 0.18	4.8
WP	26	81.68 ± 1.13	44.01 ± 1.21	0.97 ± 0.14	2.4
EP	30	18.62 ± 0.54	8.57 ± 0.32	0.19 ± 0.05	1.5
KS	14	89.66 ± 0.47	37.61 ± 0.06	−1.14 ± 0.03	1.2
TB	80	98.03 ± 0.10	37.88 ± 0.02	−0.62 ± 0.03	1.4
TS	37	66.54 ± 0.17	39.49 ± 0.05	0.77 ± 0.02	2.3
FV	39	67.93 ± 0.27	40.11 ± 0.12	0.66 ± 0.04	1.3

Note. Anticlockwise rotation is positive. See Figure 3 for block abbreviations.

Table 2
AIC and AICc Values for All 4 Block Model Scenarios

Model	*K*	WRMS (mm/yr)	AIC	AICc	Notes
1	3	4.0	200.1	200.5	One block
2A	6	2.5	140.3	141.6	Two micro-blocks, separated by SKF
2B	6	2.8	156.2	157.5	Two micro-blocks, separated by KS
3	9	2.2	115.0	118.0	Three micro-blocks, separated by SKF and KS

Note. *K* is the number of free parameters, the number of GNSS observations (*n*, see Section 4.3) in the Pamir, WRMS is the weighted root-mean-square fit to the data. See Figure 1 for fault abbreviations.

The three-block model 3 has the lowest WRMS misfit of 2.2 mm/yr and the lowest AIC and AICc values (Figure 3, Table 2), indicating that it predicts the observations well. However, there are a few stations in the Tajik basin block, close to the Darvaz fault, where the residuals are relatively large. We will discuss this discrepancy in more detail later.

The fault locking depth affects both data fit and slip rates estimates. We find that the best data fit is achieved with a locking depth of 20 or 25 km depth and that shallow locking depth fits the GNSS data worse than deep locking depth (Figure 4).

5.3. Fault Slip Rates

Our preferred three-block model 3 also provides slip rate estimates for individual fault segments (Figure 5 and Table 3). The Vakhsh thrust fault and the Illiac fault segments exhibit similar dextral slip of 10.0 ± 0.3 to 11.2 ± 0.3 mm/yr. The estimated maximum shortening across the Vakhsh fault of 7.0 ± 1.0 mm/yr decreases westward to 0.4 ± 0.5 mm/yr at the Illiac fault.

Sinistral shear of the Darvaz fault increases southwestward from 4.1 ± 0.4 mm/yr in the Peter I. Range to 7.4 ± 0.6 mm/yr at ~38°N and then to 10 ± 0.6 mm/yr along the ~NS-striking segment. The fault-perpendicular shortening rate increases from 5.3 ± 0.7 mm/yr in the northeast to 8.7 ± 0.5 mm/yr in the southwest. It is worth noting that the convergence rates across this block boundary most probably represent overall crustal shortening across several thin-skinned folds of the fold-and-thrust of the Tajik basin (Leith & Alvarez, 1985) and not the Darvaz fault only.

The western segment of the Pamir thrust system (until it connects with the Sarez-Karakul fault system) accommodates crustal convergence at a reverse dip-slip rate of approximately 8.7 ± 0.6 mm/yr (or horizontal shortening of ~8.2 mm/yr), and the eastern segment twice as much, that is ~18.3 ± 0.2 mm/yr (or horizontal shortening of ~17.2 mm/yr). Conversely, dextral shear rates dramatically drop from 9.3 ± 0.5 mm/yr at the western to ~2.2 ± 0.2 mm/yr at the eastern segment.

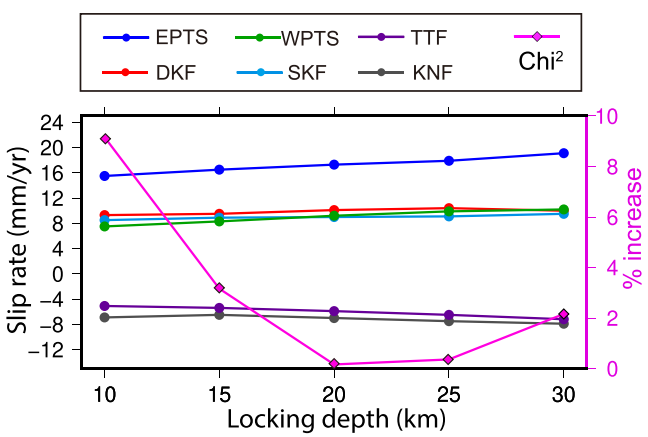

Figure 4. Slip rate variations and Chi-square increase (in percent) of different faults (see Figure 1 for abbreviations) as a function of locking depth.

In the east, the Kashgar-Yecheng transfer system seems to accommodates 2.7 ± 0.2 mm/yr of dextral shear (Figure 5) and shortening of 2.1 ± 0.1 (SE-segment) to 4.0 ± 0.2 mm/yr (NW-segment). The Sarez-Karakul fault system exhibits predominant sinistral shear from 8.8 ± 0.3 to 9.5 ± 0.2 mm/yr while extension being secondary as previously suggested (Strecker et al., 1995). Extension decreases southwestward from 3.1 ± 0.5 to 1.7 ± 0.5 mm/yr. It is worth noting that our slip rate estimates for the Sarez-Karakul fault system might include contributions from unmapped splay faults, for example, the fault that ruptured during the 2023 Mw 6.8 earthquake (R. Chen et al., 2024; Shi et al., 2023). Similar to the boundary defined by the Darvaz fault, our model is incapable of reproducing such complexity.

The predicted dextral shear on the Muji fault is 6.3 mm/yr. Its SE-continuation, the Kongur Shan normal fault, exhibits normal dip-slip of 10 ± 0.3 mm/yr (or

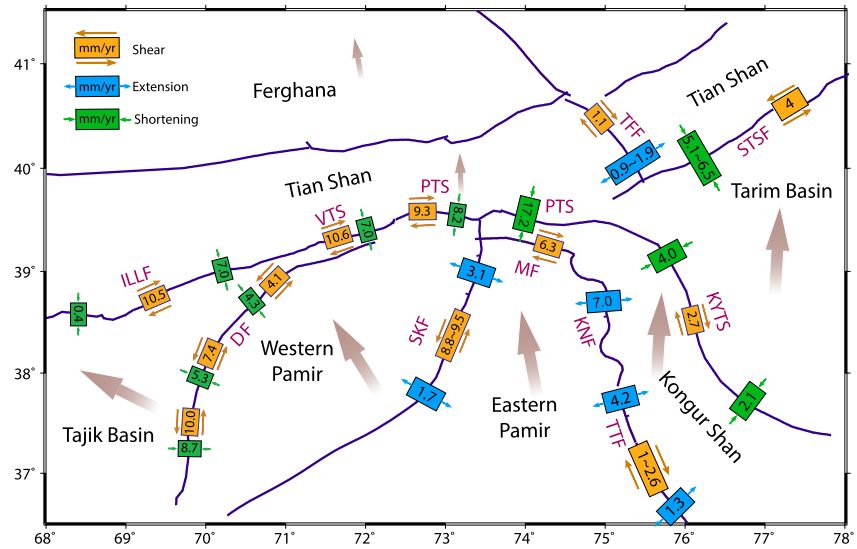

Figure 5. Fault slip rates estimates by our preferred block model 3. Blue lines mark (simplified) faults (Mohadjer et al., 2016), brown arrows show the main direction of motion relative to stable Eurasian.

extension of ~7 mm/yr) at ~38.5°N, which then gradually decreases to 5.9 ± 0.3 mm/yr (or extension of ~4.2 mm/yr) near 37.2°N and to 1.9 ± 0.2 mm/yr (or extension of ~1.3 mm/yr) along the Tashkorgan normal fault further to the southeast.

6. Discussion

6.1. Subdivision of the Pamir Into Micro-Blocks

The one-block model 1 results in a very low data misfit in the eastern Pamir but systematic residual velocities of ~10 mm/yr in the western Pamir, strongly indicating that the Pamir should be subdivided into multiple micro-blocks. The misfit decreases significantly if the Kongur Shan extensional system is considered (model 2A), but the AIC(c) values remain significantly higher than in our preferred three-block model 3 that also produces well-distinguishable Euler poles (Evans et al., 2015) (Table 2). Thus, our model suggests that the Pamir contains (at least) three crustal micro-blocks that are separated by the Sarez-Karakul fault system and the Kongur Shan extensional system. Together with the GNSS velocity cluster analysis (Figure S3 in Supporting Information S1), model 3 is in line with recent different findings of crustal seismicity and morphotectonics (Bloch et al., 2023; Schurr et al., 2014) and fault mapping on optical satellite imagery (Elliott et al., 2020) that both hypothesize a SW-extension of the Sarez-Karakul fault system (Figure S3 in Supporting Information S1).

6.2. Comparison to Previous Kinematic Models

To first order, our block model reproduces the Pamir kinematics well. The rotation pole of the Tarim basin is consistent with earlier solutions based on relatively few GNSS velocities (e.g., Loveless & Meade, 2011; Meade, 2007; Thatcher, 2007; H. Wang et al., 2011) and with those from denser GNSS velocity solutions (e.g., S. Wang et al., 2017; W. Wang et al., 2017). It also agrees with an Euler pole proposed by Avouac and Tapponnier (1993) based on geologic data. Second-order differences are caused by smaller variations in the underlying observations and block geometry definitions. For example, while Loveless and Meade (2011), Meade (2007), S. Wang et al. (2017), and W. Wang et al. (2017) defined the Kongur Shan extensional system as the western boundary of the Tarim block, we believe that the Kashgar-Yecheng transfer system is a more plausible boundary (Cowgill, 2010). As noticed by previous studies (Loveless & Meade, 2011), the small data misfit and internal deformation of the Tarim basin is consistent with the greater effective elastic thickness (Burov & Diament, 1995) and vertically averaged effective viscosity beneath the basin (Jay et al., 2017, 2018). The counterclockwise rotation of the Tajik basin is in agreement with paleomagnetic studies (Thomas et al., 1994) and with previous rotation strain rates using almost the same GNSS data set (Pan et al., 2018; Zheng et al., 2017; Zhou et al., 2016). Also, Zubovich et al. (2016) obtained an Euler vector similar to ours for the Ferghana region.

Table 3
Comparison of Fault Slip Rates Constrained by Our Preferred Block Model 3 With Published Geodetic and Geologic Slip Rates

Faults	Slip properties	This study (mm/yr)	Geologic estimates (mm/yr)	Geodetic estimates (mm/yr)
Sarez-Karakul fault system (SKF)	Sinistral shear	8.8 ± 0.3–9.5 ± 0.2	/	5 ± 2[a]
	Extension	1.7 ± 0.5–3.1 ± 0.5	/	1–3
Darvaz fault (DF)	Sinistral shear	4.1 ± 0.4 (~38.5°N)	12.5 ± 2[b], 10–15[c]	10 ± 1[d], 11[e], 11.4 ± 2[f]
		7.4 ± 0.6 (~38.0°N)		
		10 ± 0.6 (~37.5°N)		
	Shortening*	4.3 ± 0.7 (~38.5°N)	/	5–7[e]
		5.3 ± 0.7 (~38.0°N)		
		8.7 ± 0.5 (~37.5°N)		
Western Pamir thrust system (WPTS)	Dextral shear	9.3 ± 0.5	/	5.6 ± 0.8[g]
	Shortening	8.2 ± 0.6	>6[h]	12.5 ± 2.5[d], 12[e]
Eastern Pamir thrust system (EPTS)	Sinistral shear	2.2 ± 0.2	/	/
	Shortening	17.2 ± 0.3	/	17.5 ± 0.8[i], 10–15[j]
Muji fault (MF)	Dextral shear	6.3 ± 0.3	4.5 ± 0.2–11 ± 0.9[k]	9.4 ± 2.5[l]
	Extension	/	0.3–0.5[k]	/
Kongur Shan normal fault (KNF)	Dextral shear	1.2 ± 0.2	1.0[m]	/
	Extension	7.8 ± 0.3	>1.7[m], 6–8[n]	~7[d]
Tashkorgan and Taheman fault (TTF)	Dextral shear	1.0 ± 0.1–2.6 ± 0.2	>4[k]	/
	Extension	1.9 ± 0.2–5.9 ± 0.3	/	6 ± 2[e]
Kashgar-Yecheng transfer system (KYTS)	Dextral shear	2.7 ± 0.2	1.7–5.3[o]	/
	Extension	2.1 ± 0.1–4.0 ± 0.2	~5.9[p]	/
Talas Ferghana fault (TFF)	Dextral shear	1.1 ± 0.2	10 ± 2[q]	0.4 ± 2[f], 0.8 ± 0.4[i]
	Extension	0.9 ± 0.1–1.9 ± 0.2	/	/
Vakhsh thrust fault (VTF)	Dextral shear	10.1 ± 0.2–10.7 ± 0.3	13–19[r]	5[e]
	Shortening	7.0 ± 1.0	12–19[r]	10[e], 13–19[r]
South Tian Shan thrust (STST)	Sinistral shear	4.0 ± 0.3	/	~4.0[j]
	Shortening	5.1 ± 0.1–6.5 ± 0.2	5[s]	6.6 ± 0.5[i]
Illiac fault (ILLF)	Dextral shear	11.5 ± 0.3	/	8–15[r]
	Shortening	0.4 ± 0.5	/	~5[r]

Note. Extension and shortening rates are horizontal (not dip-slip). Superscripts refer to the studies listed below. *The estimated shortening rate for the DKF includes contributions from several thrust faults and folds in the Tajik basin. [a]Metzger et al. (2017). [b]Trifonov (1978, 1983). [c]Kuchai and Trifonov (1977). [d]Ischuk et al. (2013). [e]Zhou et al. (2016). [f]Mohadjer et al. (2010). [g]Zubovich et al. (2016). [h]Arrowsmith and Strecker (1999). [i]Yang et al. (2008). [j]Zubovich et al. (2010). [k]Chevalier et al. (2011). [l]Feng et al. (2017). [m]Chevalier et al. (2015). [n]J. Chen et al. (2011). [o]Sobel et al. (2011). [p]T. Li et al. (2012). [q]Burtman et al. (1996). [r]Metzger et al. (2020). [s]Scharer et al. (2004).

The modeled surface velocity field of the Pamir area clearly exhibits faster northward motion of the eastern compared to the western Pamir, and westward extrusion of the western Pamir (Figure 6a). This is in agreement with Jay et al. (2017, 2018), who derived a kinematic and dynamic surface velocity field constrained by GNSS velocities, Quaternary fault slip rates, the force balance between gravitational potential energy and the relative plate motion between India and Eurasia.

To better compare our velocity field with the one of Jay et al. (2018), we also calculate the strain rate field (Figure 6b). Significant differences between our principal strain rates and those of Jay et al. (2018) appear along the Sarez-Karakul fault system. Jay et al. (2018) excluded shear motion on the Sarez-Karakul fault system, thus their strain rates ($\sim 2.0 \times 10^{-8}$/yr) across the fault are lower than our estimation of $\sim 1.0 \times 10^{-7}$/yr. On the other hand, their strain rate across the Pamir thrust system is at least 10 times larger than ours, possibility due to the omission of back-slip on the locked fault plane (Jay et al., 2017, 2018).

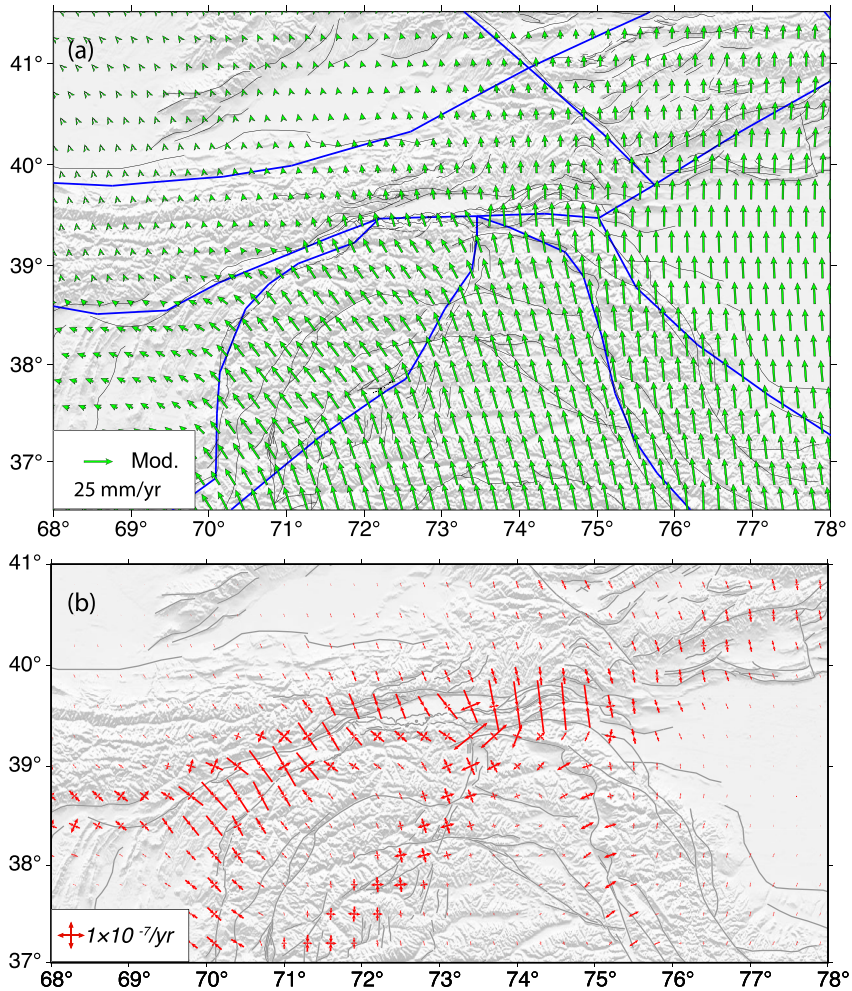

Figure 6. (a) Kinematic velocity field relative to stable Eurasia (green arrows) and (b) principal strain rates predicted by our preferred model 3. Blue lines indicate block boundaries, gray lines represent active faults (Mohadjer et al., 2016).

6.3. Geodetic and Geologic Slip Rates

The slip rates derived from our preferred block model 3 (Figure 5) generally agree well with the short- and long-term slip rates compiled in Section 2 (Figure 7 and Table 3). As already pointed out by Mohadjer et al. (2017), GNSS-derived slip rates are generally consistent with geologic slip rates in this region. Discrepancies stem from the uncertainties in each GNSS data set, variations in fault behavior over different timescales, chosen fault model geometries (Evans, 2018), and other modeling strategies. In the following, we discuss the discrepancy between slip rate constraints on the Vakhsh fault, the Darvaz fault, the Pamir thrust system, the Sarez-Karakul fault, the Muji fault and the Kongur Shan normal fault in particular.

Our estimated sinistral shear of the Vakhsh and Illiac faults is ∼10.5 mm/yr, which is somewhat smaller than the lower limit of the slip rate estimates constrained by radar interferometry (InSAR) and GNSS data (Metzger et al., 2020, 2021), while our shortening rates agrees well with their lower limit of shortening. Metzger et al. (2020) suggests that the Vakhsh fault has a very shallow locking depth, potentially even creeping at the surface. Our model (with a predefined locking depth of 20 km) produces significant residuals close to the Vakhsh fault (Figure 3c). If we reduce the locking depth of the Vakhsh fault to ∼1 km, the data fit increases, but the slip rates of the Vakhsh fault and Darvaz fault remain stable, which validates the previous suggestion of Metzger et al. (2020, 2021).

The NS-striking segment of the Darvaz fault (south of 37.8°N) seems to accommodate constant sinistral shear over geological and geodetic times (Ischuk et al., 2013; Kuchai & Trifonov, 1977; Trifonov, 1978, 1983). For the

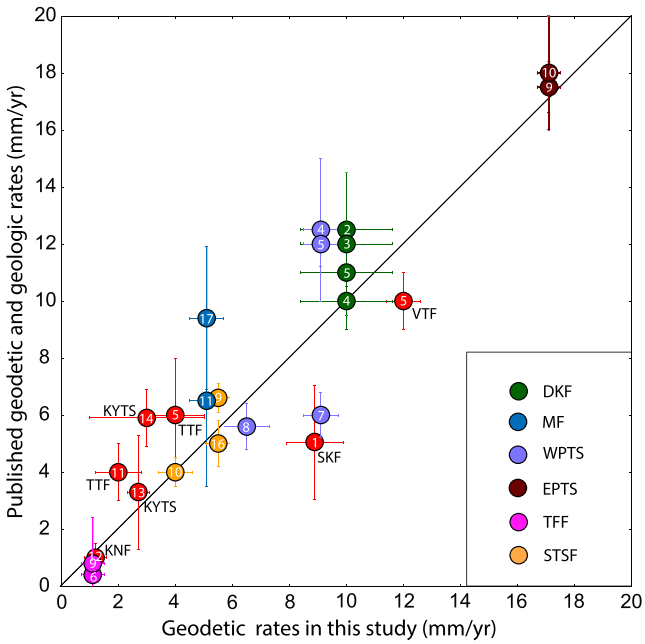

Figure 7. Geodetic slip rates (with 95% confidence intervals) derived in this study versus published geologic and geodetic estimates for the major active faults in the Pamir region (color-coded, see Figure 1 for abbreviations and Table 3 for literature references).

fault segment further north (at Peter I. Range), our model underestimates the westward outflux at Peter I. Range by ~4 mm/yr (Figure 3d) and suggests a sinistral shear three times smaller than the 15 mm/yr estimated by Metzger et al. (2020), who tailored the model such that it fits a dense cross-fault GNSS profile. Obviously, such profile models help to understand local structure complexities and provide a better data fit to a dense observation network, but they are not applicable to larger regions with inhomogeneous data distribution (Thatcher, 2009). As already discussed above, a significant fraction of the high data misfit can probably be attributed to the shallow creeping of the Vakhsh fault. In addition, it is challenging to reliably determine the strain partitioning between two closely spaced faults.

Estimates of the fault-perpendicular rates of the Darvaz fault are somewhat contradictory: Zhou et al. (2016) suggested the crustal shortening between the western Pamir and the Tajik basin, but the sparse GNSS data set did not permit to unequivocally allocate the shortening on a certain fault. Based on their dense GNSS profile across the fault, Metzger et al. (2020) suggested extension on the Darvaz fault, decreasing from 10 to ~4 mm/yr toward southwest. The latter data, however, only spans about 2 years. Our model, incorporating the survey data of Metzger et al. (2020), predicts shortening across the Darvaz fault again. However, our estimated shortening rate represents an upper limit since few near-field GNSS stations exist along the whole block boundary (Figure 3). More GNSS stations and longer time span of observations are needed to gain a better understanding of the fault-perpendicular rates and of strain partitioning across the Darvaz fault and Peter I. Range.

By comparing the average GNSS rates in the western Pamir and eastern Pamir, Metzger et al. (2017) reported the sinistral shear of 5 ± 2 mm/yr for the NNE-trending Sarez-Karakul fault system, which is less than our estimation of 8.8 ± 0.3 to 9.5 ± 0.2 mm/yr. We notice that the GNSS sites in the western Pamir are unevenly distributed and the uncertainties in the Euler pole of the western Pamir micro-block are the largest. Thus, the Euler pole reacts very sensitively to the GNSS data distribution within the micro-block. If the block boundary defined by the Sarez-Karakul fault system continues more toward S than SW (Figure S8 in Supporting Information S1), the sinistral shear on this fault decreases to ~6.5 mm/yr. Considering the geometrical uncertainties and the data sparsity in the northern part of the western Pamir block, we infer that the sinistral shear of 8.8 ± 0.3 to 9.5 ± 0.2 mm/yr probably represents the upper limit of fault slip rate at the Sarez-Karakul fault system.

At the western segment of the Pamir thrust system, the lower limit of the average reverse dip-slip of 6 mm/yr during the Holocene (Arrowsmith & Strecker, 1999) is half of the geodetic rate constrained by GNSS profiles crossing both the Pamir thrust system and the Vakhsh thrust fault further west (Ischuk et al., 2013; Zhou et al., 2016). Our shortening rate of 8.2 ± 0.6 mm/yr falls within both estimates. Our estimate of dextral shear for this segment is somewhat higher than that reported by Zubovich et al. (2016), likely due to the short distance (~5 km) of GNSS site away from the fault trace. Furthermore, our estimated crustal shortening across the eastern segment of the Pamir thrust system is comparable to the findings of Yang et al. (2008), but larger than that from previous GNSS observations by Reigber et al. (2001).

Our estimated dextral shear rate of the Muji fault (6.3 ± 0.3 mm/yr) is in agreement with geomorphologic markers (J. Chen et al., 2011; Chevalier et al., 2011; T. Li et al., 2019), but somewhat lower than that of Feng et al. (2017), who reported dextral shear of 9.4 ± 2.5 mm/yr, which might be due to unmodeled block rotations and the influence of other structures on their GNSS velocity profiles (e.g., Ge et al., 2015). The scarcity of GNSS stations in the Kongur Shan block is likely another reason for the slip rate discrepancies.

From the GNSS velocity profiles presented in Zubovich et al. (2010) and Ischuk et al. (2013), we infer that the Kongur Shan extensional system accommodates ~7.8 mm/yr of extension, consistent with our model that yields a normal dip-slip of ~10 mm/yr in the northern segment, corresponding to ~7.8 mm/yr of horizontal extension. These geodetic rates are in good agreement with Holocene estimates (J. Chen et al., 2011). It appears that the

evolution of the WNW-trending Muji fault is a result of rapid~EW-extension in the north the Kongur Shan extensional system, as both shear and extension occur at the same rate today.

6.4. Implications for Current Deformation in Pamir

The discrepancy in northward advance between the eastern and western Pamir explains the sinistral shear of the Sarez-Karakul fault system. Similar faulting mechanisms are found at the Talas-Ferghana fault, separating the western Tian Shan and central Tian Shan, and the Piqiang fault (Figure 1; J. Li et al., 2022; Turner et al., 2011). Dextral shear on the western segment of the Pamir thrust system results from the counterclockwise rotation and westward extrusion of the western Pamir that gravitationally collapses into the Tajik-Afghan depression (Schurr et al., 2014). In the eastern Pamir, eastward extrusion is less obvious. Radial thrusting and gravitational collapse (e.g., Robinson et al., 2004, 2007) appear to be the most plausible mechanisms for extension in this region (Figure 7). Our preferred block model and the strike-slip earthquakes in 1911 (M 7.3) and 2023 (Mw 6.8) on the Pamir plateau suggest that the shear zone is either much longer (toward southwest, Elliott et al., 2020) and/or much wider (Kulikova et al., 2016; Shi et al., 2023) than previously thought.

7. Conclusions

The most comprehensive GNSS velocity solution of the region to date provides an unprecedented insight into the kinematics of the Pamir and adjacent areas. Using elastic micro-block modeling we constrain Euler poles, velocity and strain fields, and fault slip rates of the major active blocks and faults bounding and dividing the orogen. Our preferred model confirms the separation of the western and eastern Pamir along the NNE-trending sinistral strike-slip Sarez-Karakul fault system proposed earlier (Rutte et al., 2017; Schurr et al., 2014; Stübner et al., 2013) and suggests a third micro-block defined by the SSE-trending Kongur Shan extensional system.

Our results show relatively minor extension compared to significant shear along the Sarez-Karakul fault system, thus supporting the hypothesis of bulk northward motion of the eastern Pamir and the westward extrusion of the western Pamir (Metzger et al., 2017; Schurr et al., 2014). From the GNSS observations we infer that the northern segments of both the Sarez-Karakul fault system and the Kongur Shan extensional system are accommodating ~EW extension across the Pamir plateau. Our model also validates the presumed southwestward extension of the Sarez-Karakul fault system (Elliott et al., 2020), but the exact fault trace remains difficult to constrain given the GNSS data sparsity. High-resolution InSAR velocity maps might solve this issue in the future.

Data Availability Statement

Survey-mode RINEX data of the Afghan Hindu Kush and western Pamir margin are available at GFZ Data Services (https://doi.org/10.5880/GFZ.4.1.2019.007, https://doi.org/10.5880/GFZ.4.1.2021.003) (Metzger et al., 2019, 2021). The integrated GNSS velocities analyzed in this study can be are archived at Zenodo (https://zenodo.org/records/13870599) (D. Wang et al., 2024).

Acknowledgments
We kindly thank Roland Bürgmann, Marie-Luce Chevalier and Jeffrey T. Freymueller for their valuable suggestions to improve the initial manuscript. The authors also thank reviewers for their comments and suggestions. This work was supported by the National Key R&D Program of China (2022YFC3003703), Key R&D Program of Xinjiang Uygur Autonomous Region (2020B03006-2), the National Nature Science Foundation of China (42274014, 41974004), the Royal Society Grant NIF\R1\201854 (UK), and China Postdoctoral Science Foundation (BX20200250, 2021M700100). GNSS data were processed using GAMIT/GLOBK package. Figures were prepared using GMT mapping tools (Wessel et al., 2013).

References

Akaike, H. (1974). A new look at the statistical model identification. *IEEE Transactions on Automatic Control*, *19*(6), 716–723. https://doi.org/10.1109/TAC.1974.1100705

Altamimi, Z., Métivier, L., Rebischung, P., Rouby, H., & Collilieux, X. (2017). ITRF2014 plate motion model. *Geophysical Journal International*, *209*(3), 1906–1912. https://doi.org/10.1093/gji/ggx136

Altamimi, Z., Rebischung, P., Métivier, L., & Collilieux, X. (2016). ITRF2014: A new release of the international terrestrial reference frame modeling non-linear station motions. *Journal of Geophysical Research: Solid Earth*, *121*(8), 6109–6131. https://doi.org/10.1002/2016JB013098

Arrowsmith, J. R., & Strecker, M. R. (1999). Seismotectonic range-front segmentation and mountain-belt growth in the Pamir-Alai region, Kyrgyzstan (India-Eurasia collision zone). *GSA Bulletin*, *111*(11), 1665–1683. https://doi.org/10.1130/0016-7606(1999)111<1665:SRFSAM>2.3.CO;2

Avouac, J.-P., & Tapponnier, P. (1993). Kinematic model of active deformation in central Asia. *Geophysical Research Letters*, *20*(10), 895–898. https://doi.org/10.1029/93gl00128

Bird, P. (2003). An updated digital model of plate boundaries. *Geochemistry, Geophysics, Geosystems*, *4*(3), 1027. https://doi.org/10.1029/2001GC000252

Bloch, W., Metzger, S., Schurr, B., Yuan, X., Ratschbacher, L., Reuter, S., et al. (2023). The 2015-2017 Pamir earthquake sequence: Foreshocks, main shocks and aftershocks, seismotectonics, fault interaction and fluid processes. *Geophysical Journal International*, *233*(1), 641–662. https://doi.org/10.1093/gji/ggac473

Burov, E. B., & Diament, M. (1995). The effective elastic thickness (Te) of continental lithosphere: What does it really mean? *Journal of Geophysical Research*, *100*(B3), 3905–3927. https://doi.org/10.1029/94jb02770

Burtman, V. S., & Molnar, P. (1993). Geological and geophysical evidence for deep subduction of continental crust beneath the Pamir. *Geological Society of America Special Papers*, 1–76. https://doi.org/10.1130/spe281-p1

Burtman, V. S., Skobelev, S. F., & Molnar, P. (1996). Late Cenozoic slip on the Talas-Ferghana fault, the Tien Shan, central Asia. *Geological Society of America Bulletin*, *108*, 1004–1021. https://doi.org/10.1130/0016-7606(1996)108

Chen, J., Schomenbohm, L. M., Yuan, Z., Li, T., Owen, L., Sobel, E. R., et al. (2011). Holocene slip rate along the northern Kongur Extensional System, Chinese Pamir. In *AGU fall meeting*. Abstract, T43f-2447.

Chen, R., Li, J., Liu, D., Yushan, A., Li, R., & Kong, X. (2024). InSAR coseismic deformation and seismogenic structure of the 2023 Mw6.9 Tajikistan earthquake. *Geodesy and Geodynamics*. https://doi.org/10.1016/j.geog.2023.12.004

Chevalier, M. L., Li, H., Pan, J., Pei, J., Wu, F., Xu, W., et al. (2011). Fast slip-rate along the northern end of the Karakorum fault system, western Tibet. *Geophysical Research Letters*, *38*(22), 1–7. https://doi.org/10.1029/2011GL049921

Chevalier, M. L., Pan, J., Li, H., Liu, D., & Wang, M. (2015). Quantification of both normal and right-lateral late Quaternary activity along the Kongur Shan extensional system, Chinese Pamir. *Terra Nova*, *27*(5), 379–391. https://doi.org/10.1111/ter.12170

Coutand, I., Strecker, M. R., Arrowsmith, J. R., Hilley, G., Thiede, R. C., Korjenkov, A., & Omuraliev, M. (2002). Late Cenozoic tectonic development of the intramontane Alai Valley, (Pamir-Tien Shan region, central Asia): An example of intracontinental deformation due to the Indo-Eurasia collision. *Tectonics*, *21*(6). https://doi.org/10.1029/2002TC001358

Cowgill, E. (2010). Cenozoic right-slip faulting along the eastern margin of the Pamir salient, northwestern China. *GSA Bulletin*, *122*(1–2), 145–161. https://doi.org/10.1130/B26520.1

d'Alessio, M. A., Johanson, I. A., Bürgmann, R., Schmidt, D. A., & Murray, M. H. (2005). Slicing up the San Francisco Bay Area: Block kinematics and fault slip rates from GPS-derived surface velocities. *Journal of Geophysical Research*, *110*(B6), B06403. https://doi.org/10.1029/2004JB003496

Ekström, G., Nettles, M., & Dziewonski, A. M. (2012). The global CMT project 2004-2010: Centroid-moment tensors for 13,017 earthquakes. *Physics of the Earth and Planetary Interiors*, *200–201*, 1–9. https://doi.org/10.1016/j.pepi.2012.04.002

Elliott, A., Elliott, J., Hollingsworth, J., Kulikova, G., Parsons, B., & Walker, R. (2020). Satellite imaging of the 2015 M7.2 earthquake in the Central Pamir, Tajikistan, elucidates a sequence of shallow strike-slip ruptures of the Sarez-Karakul fault. *Geophysical Journal International*, *221*(3), 1696–1718. https://doi.org/10.1093/GJI/GGAA090

Evans, E. L. (2018). A comprehensive analysis of geodetic slip-rate estimates and uncertainties in California. *Bulletin of the Seismological Society of America*, *108*(1), 1–18. https://doi.org/10.1785/0120170159

Evans, E. L., Loveless, J. P., & Meade, B. J. (2015). Total variation regularization of geodetically and geologically constrained block models for the western United States. *Geophysical Journal International*, *202*(2), 713–727. https://doi.org/10.1093/gji/ggv164

Feng, W., Tian, Y., Zhang, Y., Samsonov, S., Almeida, R., & Liu, P. (2017). A slip gap of the 2016 Mw 6.6 Muji, Xinjiang, China, earthquake inferred from Sentinel-1 TOPS interferometry. *Seismological Research Letters*, *88*(4), 1054–1064. https://doi.org/10.1785/0220170019

Ge, W. P., Molnar, P., Shen, Z. K., & Li, Q. (2015). Present-day crustal thinning in the southern and northern Tibetan Plateau revealed by GPS measurements. *Geophysical Research Letters*, *42*(13), 5227–5235. https://doi.org/10.1002/2015GL064347

Guseva, T. G. (1986). *Contemporary movements of the Earth's crust in the transition zone from the Pamir to the Tien Shan (in Russian)* (p. 171). Institute of Physics of the Earth, Russian Academy of Sciences.

Herring, T. A., King, R. W., Floyd, M. A., & McClusky, S. C. (2018). *Introduction to GAMIT/GLOBK, Release 10.7, Technical Report*. Department of Earth, Atmospheric, and Planetary Sciences, Massachussetts Institute Technology.

Ischuk, A., Bendick, R., Rybin, A., Molnar, P., Khan, S. F., Kuzikov, S., et al. (2013). Kinematics of the Pamir and Hindu Kush regions from GPS geodesy. *Journal of Geophysical Research: Solid Earth*, *118*(5), 2408–2416. https://doi.org/10.1002/jgrb.50185

Jay, C. N., Flesch, L. M., & Bendick, R. O. (2017). Kinematics and dynamics of the Pamir, central Asia: Quantifying surface deformation and force balance in an intracontinental subduction zone. *Journal of Geophysical Research: Solid Earth*, *122*(6), 4741–4762. https://doi.org/10.1002/2017JB014177

Jay, C. N., Flesch, L. M., & Bendick, R. O. (2018). Kinematics and dynamics of the Pamir, central Asia: Quantifying the roles of continental subduction in force balance. *Journal of Geophysical Research: Solid Earth*, *123*(9), 8161–8179. https://doi.org/10.1029/2018JB015615

Jouanne, F., Awan, A., Pecher, A., Kausar, A., Mugnier, J. L., Khan, I., et al. (2014). Present-day deformation of northern Pakistan from Salt Ranges to Karakorum Ranges. *Journal of Geophysical Research: Solid Earth*, *119*(3), 2487-–2503. https://doi.org/10.1002/2013JB010776

Konolpatsev, I. M. (1971). Measurements of crustal movements in the Garm area, 1948-1970. *Geotektonika*, *5*, 111–116. (in Russian).

Kuchai, V., & Trifonov, V. G. (1977). Young left-lateral strike slip along the zone of the Darvaz. *Geotektonika*, *3*, 91-–105.

Kufner, S. K., Kakar, N., Bezada, M., Bloch, W., Metzger, S., Yuan, X., et al. (2021). The Hindu Kush slab break-off as revealed by deep structure and crustal deformation. *Nature Communications*, *12*(1), 1685. https://doi.org/10.1038/s41467-021-21760-w

Kufner, S. K., Schurr, B., Ratschbacher, L., Murodkulov, S., Abdulhameed, S., Ischuk, A., et al. (2018). Seismotectonics of the Tajik Basin and surrounding mountain ranges. *Tectonics*, *37*(8), 2404–2424. https://doi.org/10.1029/2017TC004812

Kufner, S. K., Schurr, B., Sippl, C., Yuan, X., Ratschbacher, L., Ischuk, A., et al. (2016). Deep India meets deep Asia: Lithospheric indentation, delamination and break-off under Pamir and Hindu Kush (central Asia). *Earth and Planetary Science Letters*, *435*(February), 171–184. https://doi.org/10.1016/j.epsl.2015.11.046

Kulikova, G., Schurr, B., Krüger, F., Brzoska, E., & Heimann, S. (2016). Source parameters of the Sarez-Pamir earthquake of 1911 February 18. *Geophysical Journal International*, *205*(2), 1086–1098. https://doi.org/10.1093/gji/ggw069

Lagler, K., Schindelegger, M., Böhm, J., Krásná, H., & Nilsson, T. (2013). GPT2: Empirical slant delay model for radio space geodetic techniques. *Geophysical Research Letters*, *40*(6), 1069–1073. https://doi.org/10.1002/grl.50288

Leith, W., & Alvarez, W. (1985). Structure of the Vakhsh fold-and-thrust belt, Tadjik SSR: Geologic mapping on a Landsat image base. *Geological Society of America Bulletin*, *96*(7), 875–885. https://doi.org/10.1130/0016-7606(1985)96<875:SOTVFB>2.0.CO;2

Li, J., Yao, Y., Li, R., Yusan, S., Li, G., Freymueller, J. T., & Wang, Q. (2022). Present-Day strike-slip faulting and thrusting of the Kepingtage fold-and-thrust belt in southern Tianshan: Constraints from GPS observations. *Geophysical Research Letters*, *49*(11), 1–11. https://doi.org/10.1029/2022gl099105

Li, T., Chen, J., Thompson, J. A., Burbank, D. W., & Xiao, W. (2012). Equivalency of geologic and geodetic rates in contractional orogens: New insights from the Pamir Frontal Thrust. *Geophysical Research Letters*, *39*(15), 1–6. https://doi.org/10.1029/2012GL051782

Li, T., Schoenbohm, L. M., Chen, J., Yuan, Z., Feng, W., Li, W., et al. (2019). Cumulative and coseismic (during the 2016 Mw 6.6 Aketao earthquake) deformation of the dextral-slip Muji Fault, northeastern Pamir orogen. *Tectonics*, *38*(11), 3975–3989. https://doi.org/10.1029/2019TC005680

Loveless, J. P., & Meade, B. J. (2011). Partitioning of localized and diffuse deformation in the Tibetan Plateau from joint inversions of geologic and geodetic observations. *Earth and Planetary Science Letters*, *303*(1–2), 11–24. https://doi.org/10.1016/j.epsl.2010.12.014

McCaffrey, R. (2005). Block kinematics of the Pacific–North America plate boundary in the southwestern United States from inversion of GPS, seismological, and geologic data. *Journal of Geophysical Research*, *110*(B7), B07401. https://doi.org/10.1029/2004JB003307
Meade, B. J. (2007). Present-day kinematics at the India-Asia collision zone. *Geology*, *35*(1), 81–84. https://doi.org/10.1130/G22924A.1
Meade, B. J., & Hager, B. H. (2005). Spatial localization of moment deficits in southern California. *Journal of Geophysical Research*, *110*(4), 1–6. https://doi.org/10.1029/2004JB003331
Meade, B. J., & Loveless, J. P. (2009). Block modeling with connected fault-network geometries and a linear elastic coupling estimator in spherical coordinates. *Bulletin of the Seismological Society of America*, *99*(6), 3124–3139. https://doi.org/10.1785/0120090088
Metzger, S., Ischuk, A., Akhmedov, A., Ilyasova, Z., Moreno, M., Murodkulov, S., & Deng, Z. (2019). Survey mode GPS data in the West Pamir, Tajikistan, central Asia, 2013–2016 [Dataset]. *GFZ Data Services*. https://doi.org/10.5880/GFZ.4.1.2019.007
Metzger, S., Ischuk, A., Deng, Z., Ratschbacher, L., Perry, M., Kufner, S. K., et al. (2020). Dense GNSS profiles across the northwestern tip of the India-Asia collision zone: Triggered slip and westward flow of the Peter the First Range, Pamir, into the Tajik Depression. *Tectonics*, *39*(2), 1–20. https://doi.org/10.1029/2019TC005797
Metzger, S., Kakar, N., Zubovich, A., Borisov, M., Saif, S., Panjsheri, A. H., et al. (2021). Survey mode GNSS data, acquired 2014–2019 in the Afghan Hindu Kush and across northern Pamir margin, central Asia [Dataset]. *GFZ Data Services*. https://doi.org/10.5880/GFZ.4.1.2021.003
Metzger, S., Schurr, B., Ratschbacher, L., Sudhaus, H., Kufner, S. K., Schöne, T., et al. (2017). The 2015 Mw7.2 Sarez strike-slip earthquake in the Pamir interior: Response to the underthrusting of India's western promontory. *Tectonics*, *36*(11), 2407–2421. https://doi.org/10.1002/2017TC004581
Mohadjer, S., Bendick, R., Ischuk, A., Kuzikov, S., Kostuk, A., Saydullaev, U., et al. (2010). Partitioning of India-Eurasia convergence in the Pamir-Hindu Kush from GPS measurements. *Geophysical Research Letters*, *37*(4), 1–6. https://doi.org/10.1029/2009GL041737
Mohadjer, S., Ehlers, T. A., Bendick, R., & Mutz, S. G. (2017). Review of GPS and Quaternary fault slip rates in the Himalaya-Tibet orogen. *Earth-Science Reviews*, *174*, 39–52. https://doi.org/10.1016/j.earscirev.2017.09.005
Mohadjer, S., Ehlers, T. A., Bendick, R., Stübner, K., & Strube, T. (2016). A Quaternary fault database for central Asia. *Natural Hazards and Earth System Sciences*, *16*(2), 529–542. https://doi.org/10.5194/nhess-16-529-2016
Nikolaev, V. G. (2002). Afghan-Tajik depression: Architecture of sedimentary cover and evolution. *Russian Journal of Earth Sciences*, *4*(6), 399–421. https://doi.org/10.2205/2002es000106
Okada, Y. (1985). Surface deformation due to shear and tensile faults in a half-space. *Bulletin of the Seismological Society of America*, *75*(4), 1135–1154. https://doi.org/10.1785/bssa0750041135
Pan, Z., He, J., & Li, J. (2018). Contemporary crustal deformation within the Pamir plateau constrained by geodetic observations and focal mechanism solutions. *Pure and Applied Geophysics*, *175*(10), 3463–3484. https://doi.org/10.1007/s00024-018-1872-3
Perry, M., Kakar, N., Ischuk, A., Metzger, S., Bendick, R., Molnar, P., & Mohadjer, S. (2019). Little geodetic evidence for localized Indian subduction in the Pamir-Hindu Kush of central Asia. *Geophysical Research Letters*, *46*(1), 109–118. https://doi.org/10.1029/2018GL080065
Reigber, C., Michel, G. W., Galas, R., Angermann, D., Klotz, J., Chen, J. Y., et al. (2001). New space geodetic constraints on the distribution of deformation in central Asia. *Earth and Planetary Science Letters*, *191*(1–2), 157–165. https://doi.org/10.1016/S0012-821X(01)00414-9
Robinson, A. C., Yin, A., Manning, C. E., Harrison, T. M., Zhang, S. H., & Wang, X. F. (2004). Tectonic evolution of the northeastern Pamir: Constraints from the northern portion of the Cenozoic Kongur Shan extensional system, western China. *Geological Society of America Bulletin*, *116*(7–8), 953–973. https://doi.org/10.1130/B25375.1
Robinson, A. C., Yin, A., Manning, C. E., Harrison, T. M., Zhang, S. H., & Wang, X. F. (2007). Cenozoic evolution of the eastern Pamir: Implications for strain-accommodation mechanisms at the western end of the Himalayan-Tibetan orogen. *GSA Bulletin*, *119*(7–8), 882–896. https://doi.org/10.1130/B25981.1
Rutte, D., Ratschbacher, L., Schneider, S., Stübner, K., Stearns, M. A., Gulzar, M. A., & Hacker, B. R. (2017). Building the Pamir-Tibetan Plateau—Crustal stacking, extensional collapse, and lateral extrusion in the Central Pamir: 1. Geometry and kinematics. *Tectonics*, *36*(3), 342–384. https://doi.org/10.1002/2016TC004293
Sangha, S., Peltzer, G., Zhang, A., Meng, L., Liang, C., Lundgren, P., & Fielding, E. (2017). Fault geometry of 2015, Mw7.2 Murghab, Tajikistan earthquake controls rupture propagation: Insights from InSAR and seismological data. *Earth and Planetary Science Letters*, *462*, 132–141. https://doi.org/10.1016/j.epsl.2017.01.018
Sass, P., Ritter, O., Ratschbacher, L., Tympel, J., Matiukov, V. E., Rybin, A. K., & Batalev, V. Y. (2014). Resistivity structure underneath the Pamir and southern Tian Shan. *Geophysical Journal International*, *198*(1), 564–579. https://doi.org/10.1093/gji/ggu146
Scharer, K. M., Burbank, D. W., Chen, J., Weldon, R. J., Rubin, C., Zhao, R., & Shen, J. (2004). Detachment folding in the southwestern Tian Shan-Tarim foreland, China: Shortening estimates and rates. *Journal of Structural Geology*, *26*(11), 2119–2137. https://doi.org/10.1016/j.jsg.2004.02.016
Schneider, F. M., Yuan, X., Schurr, B., Mechie, J., Sippl, C., Haberland, C., et al. (2013). Seismic imaging of subducting continental lower crust beneath the Pamir. *Earth and Planetary Science Letters*, *375*, 101–112. https://doi.org/10.1016/j.epsl.2013.05.015
Schurr, B., Ratschbacher, L., Sippl, C., Gloaguen, R., Yuan, X., & Mechie, J. (2014). Seismotectonics of the Pamir. *Tectonics*, *33*(8), 1501–1518. https://doi.org/10.1002/2014TC003576
Shen, Z., Lu, J., Wang, M., & Bürgmann, R. (2005). Contemporary crustal deformation around the southeast borderland of the Tibetan Plateau. *Journal of Geophysical Research*, *110*(B11), 1–17. https://doi.org/10.1029/2004JB003421
Shi, Y., Wang, Y., & Bian, Y. (2023). Coseismic source model of the February 2023 Mw 6.8 Tajikistan earthquake from Sentinel-1A InSAR observations and its associated earthquake hazard. *Remote Sensing*, *15*(12), 1–12. https://doi.org/10.3390/rs15123010
Simpson, R. W., Thatcher, W., & Savage, J. C. (2012). Using cluster analysis to organize and explore regional GPS velocities. *Geophysical Research Letters*, *39*(17), 1–5. https://doi.org/10.1029/2012GL052755
Sippl, C., Schurr, B., Tympel, J., Angiboust, S., Mechie, J., Yuan, X., et al. (2013). Deep burial of Asian continental crust beneath the Pamir imaged with local earthquake tomography. *Earth and Planetary Science Letters*, *384*, 165–177. https://doi.org/10.1016/j.epsl.2013.10.013
Sobel, E. R., Schoenbohm, L. M., Chen, J., Thiede, R., Stockli, D. F., Sudo, M., & Strecker, M. R. (2011). Late Miocene-Pliocene deceleration of dextral slip between Pamir and Tarim: Implications for Pamir orogenesis. *Earth and Planetary Science Letters*, *304*(3–4), 369–378. https://doi.org/10.1016/j.epsl.2011.02.012
Strecker, M. R., Frisch, W., Hamburger, M. W., Ratschbacher, L., Semiletkin, S., Zamoruyev, A., & Sturchio, N. (1995). Quaternary deformation in the eastern Pamirs, Tadzhikistan and Kyrgyzstan. *Tectonics*, *14*(5), 1061–1079. https://doi.org/10.1029/95TC00927
Stübner, K., Ratschbacher, L., Weise, C., Chow, J., Hofmann, J., Khan, J., et al. (2013). The giant Shakhdara migmatitic gneiss dome, Pamir, India-Asia collision zone: 2. Timing of dome formation. *Tectonics*, *32*(5), 1404–1431. https://doi.org/10.1002/tect.20059
Thatcher, W. (2007). Microplate model for the present-day deformation of Tibet. *Journal of Geophysical Research*, *112*(B1), B01401. https://doi.org/10.1029/2005JB004244

Thatcher, W. (2009). How the continents deform: The evidence from tectonic geodesy. *Annual Review of Earth and Planetary Sciences*, *37*(1), 237–262. https://doi.org/10.1146/annurev.earth.031208.100035

Thomas, J.-C., Chauvin, A., Gapais, D., Bazhenov, M. L., Perroud, H., Cobbold, P. R., & Burtman, V. S. (1994). Paleomagnetic evidence for Cenozoic block rotations in the Tadjik depression (central Asia). *Journal of Geophysical Research*, *99*(B8), 15141–15160. https://doi.org/10.1029/94jb00901

Trifonov, V. G. (1978). Late Quaternary tectonic movements of western and central Asia. *Bulletin of the Geological Society of America*, *89*(7), 1059–1072. https://doi.org/10.1130/0016-7606(1978)89<1059:LQTMOW>2.0.CO;2

Trifonov, V. G. (1983). *The late quaternary tectogenesis*. Nauka.

Turner, S. A., Liu, J. G., & Cosgrove, J. W. (2011). Structural evolution of the Piqiang fault zone, NW Tarim Basin, China. *Journal of Asian Earth Sciences*, *40*(1), 394–402. https://doi.org/10.1016/j.jseaes.2010.06.005

Wang, D., Zhao, B., Li, J., & Metzger, S. (2024). An integrated GNSS velocity field in the Pamir, central Asia [Dataset]. *Zenodo*. https://zenodo.org/records/13870599

Wang, H., Liu, M., Cao, J., Shen, X., & Zhang, G. (2011). Slip rates and seismic moment deficits on major active faults in mainland China. *Journal of Geophysical Research*, *116*, 1–17. https://doi.org/10.1029/2010JB007821

Wang, S., Xu, C., Wen, Y., Yin, Z., Jiang, G., & Fang, L. (2017). Slip model for the 25 November 2016 Mw 6.6 Aketao earthquake, western China, revealed by Sentinel-1 and ALOS-2 observations. *Remote Sensing*, *9*(4), 325. https://doi.org/10.3390/rs9040325

Wang, W., Qiao, X., Yang, S., & Wang, D. (2017). Present-day velocity field and block kinematics of Tibetan Plateau from GPS measurements. *Geophysical Journal International*, *208*(2), 1088–1102. https://doi.org/10.1093/gji/ggw445

Wessel, P., Smith, W. H. F., Scharroo, R., Luis, J., & Wobbe, F. (2013). Generic mapping tools: Improved version released. *Eos, Transactions American Geophysical Union*, *94*(45), 409–410. https://doi.org/10.1002/2013EO450001

Xu, X., Wen, X., Chen, G., & Yu, G. (2008). Discovery of the Longriba fault zone in eastern Bayan Har block, China and its tectonic implication. *Science in China—Series D: Earth Sciences*, *51*(9), 1209–1223. https://doi.org/10.1007/s11430-008-0097-1

Yang, S. M., Li, J., & Wang, Q. (2008). The deformation pattern and fault rate in the Tianshan Mountains inferred from GPS observations. *Science in China—Series D: Earth Sciences*, *51*(8), 1064–1080. https://doi.org/10.1007/s11430-008-0090-8

Zhao, B., Huang, Y., Zhang, C., Wang, W., Tan, K., & Du, R. (2015). Crustal deformation on the Chinese mainland during 1998–2014 based on GPS data. *Geodesy and Geodynamics*, *6*(1), 7–15. https://doi.org/10.1016/j.geog.2014.12.006

Zheng, G., Wang, H., Wright, T. J., Lou, Y., Zhang, R., Zhang, W., et al. (2017). Crustal deformation in the India-Eurasia collision zone from 25 years of GPS measurements. *Journal of Geophysical Research: Solid Earth*, *122*(11), 9290–9312. https://doi.org/10.1002/2017JB014465

Zhou, Y., He, J., Oimahmadov, I., Gadoev, M., Pan, Z., Wang, W., et al. (2016). Present-day crustal motion around the Pamir Plateau from GPS measurements. *Gondwana Research*, *35*, 144–154. https://doi.org/10.1016/j.gr.2016.03.011

Zubovich, A., Metzger, S., Schöne, T., Kley, J., Mosienko, O., Zech, C., et al. (2022). Cyclic fault slip under the magnifier: Co- and postseismic response of the Pamir front to the 2015 Mw7.2 Sarez, Central Pamir, earthquake. *Tectonics*, *41*(9). https://doi.org/10.1029/2022TC007213

Zubovich, A., Schöne, T., Metzger, S., Mosienko, O., Mukhamediev, S., Sharshebaev, A., & Zech, C. (2016). Tectonic interaction between the Pamir and Tien Shan observed by GPS. *Tectonics*, *35*(2), 283–292. https://doi.org/10.1002/2015TC004055

Zubovich, A. V., Wang, X. Q., Scherba, Y. G., Schelochkov, G. G., Reilinger, R., Reigber, C., et al. (2010). GPS velocity field for the Tien Shan and surrounding regions. *Tectonics*, *29*(6), 1–23. https://doi.org/10.1029/2010TC002772